Appl Phys A (2013) 111:711–717
DOI 10.1007/s00339-013-7647-x

Applied Physics A
Materials Science & Processing

RAPID COMMUNICATION

Porosity-moderated ultrafast electron transport in Au nanowire networks

Evaggelos Magoulakis · Athanasia Kostopoulou · Georgios N. Arvanitakis · Antonios G. Kanaras · Antonis N. Andriotis · Alexandros Lappas · Panagiotis A. Loukakos

Received: 19 November 2012 / Accepted: 23 February 2013 / Published online: 27 March 2013

Abstract We demonstrate for first time the ultrafast properties of a newly formed porous Au nanostructure. The properties of the porous nanostructure are compared with those of a solid gold film using time-resolved optical spectroscopy. The experiments suggest that under the same excitation conditions the relaxation dynamics are slower in the former. Our observations are evaluated by simulations based on a phenomenological rate equation model. The impeded dynamics has been attributed to the porous nature of the structure in the networks, which results in reduced efficiency during the dissipation of the laser-deposited energy. Importantly, the porosity of the complex three-dimensional nanostructure is introduced as a geometrical control parameter of its ultrafast electron transport.

E. Magoulakis · A. Kostopoulou · G.N. Arvanitakis · A.N. Andriotis · A. Lappas · P.A. Loukakos (✉)
Foundation for Research and Technology—Hellas, Institute of Electronic Structure and Laser, N. Plastira 100, P.O. Box 1385, 71110 Heraklion, Greece
e-mail: loukakos@iesl.forth.gr
Fax: +30-2810-391305

E. Magoulakis · G.N. Arvanitakis
Physics Department, University of Crete, P.O. Box 2208, 71409 Heraklion, Greece

A. Kostopoulou
Chemistry Department, University of Crete, Voutes, 71003 Heraklion, Greece

A.G. Kanaras
Physics & Astronomy, University of Southampton, Southampton SO17 1BJ, Hants, UK

1 Introduction

Understanding the optical properties and ultrafast electron interactions of complex inorganic nanostructures is a research area of great interest. The main reason is that the properties of materials at the nanoscale are different from their bulk counterparts [1, 2]. Metallic and semiconducting nanostructures are of particular importance due to possible applications as switches or interconnecting elements in nanocircuits [3], components in photovoltaic cells [4, 5], and catalysts [6].

When the scale of matter is reduced to sizes comparable to or smaller than the electron mean free path (about 100 nm for Au at room temperature [7]), the optical properties and ultrafast electron dynamics may change drastically. Using excitation by ultrashort laser pulses, and in the sub-ps time scale, Voisin et al. [8, 9] have shown that for nanoparticles larger than 10 nm, the electron–electron (e-e) thermalization times are close to the bulk ones, while for smaller nanoparticles they sharply decrease. In the ps time scale, Stagira et al. [10] and Stella et al. [11] have observed a dependence of the electron–phonon (e-ph) interaction on the nanoparticle size. This dependence was attributed to the contribution of the surface phonons to the e-ph scattering as well as the increased surface/volume ratio with decreasing size. Other studies have shown that electron transport as well is critically affected by the size of matter [12]. At larger temporal windows (in the time scale of ∼100 ps), the thermalized electron-lattice system cools down through heat transport to the surrounding medium [13]. These studies have shown the importance of nanoparticle size reduction and the resulting spatially isotropic electron confinement on the fundamental ultrafast electron interactions.

In addition to their size, the shape of the nanoparticles also affects the ultrafast electron dynamics of the

material [2]. Therefore, research regarding electron confinement in anisotropic nanostructures is increasingly pursued [1, 14, 15]. Recent developments in the growth of more complex, three-dimensional nanostructures [16–18] have shown the way for potential applications in nanodevices, nanocatalysis, nanofoams in composite materials [16, 19–21], and drug delivery [22]. In such nanomaterials, several open questions emerge pertinent to whether and how the ultrafast dynamical properties will depend on the peculiar shape and structure that in turn may lead to nonisotropic boundary conditions and electron confinement [1]. These altered properties may drastically influence the macroscopic electrical, optical, and mechanical behavior of the material, thus affecting its performance in relevant applications.

In particular, when Au nanowire networks (NWNs) is the material of interest, the ultrafast electron interactions, following ultrashort laser excitation, have not been studied so far. Because of the unconventional shape and morphology of the nanostructure, it becomes increasingly difficult to define the relevant parameters that govern the ultrafast electron dynamics. It is the main objective of the present work to identify those nanoscale morphological characteristics, which play a crucial role during the evolution of such ultrafast processes.

In view of understanding ultrafast phenomena in relevant materials we have developed for the first time a simple chemical approach that affords surfactant-free Au three-dimensional (3D) colloidal NWNs, and we studied their ultrafast dynamics by utilizing ultrafast pump-probe spectroscopy. We found a transient modulation in their transmission that is induced by the laser excitation. In particular, it is shown that the recovery of the transmissivity to the equilibrium value (i.e., to the state prior laser excitation) is slower in the Au NWNs when it is compared to Au thin films (TFs). The results suggest a reduced efficiency in the energy dissipation. Based on phenomenological simulations, we attribute these observations not only to increased electron confinement, but also to the porous features imposed by the characteristic nanowire network morphology. Thus, we demonstrate and introduce for the first time the significance of the morphological parameter of porosity in the determination of the ultrafast optoelectronic properties of such complex, porous nanostructures.

2 Experimental section

Our synthetic approach incorporates a simplified protocol, which has not been reported before, and affords surfactant-free Au-NWNs in aqueous media. Au NWNs with a total average diameter of ~100 nm were prepared directly into water by the reduction of the $HAuCl_4 \times 3H_2O$ gold precursor from $NaBH_4$. Our approach is fundamentally different from that in earlier literature [16] as no surface capping agents are employed during the chemical synthesis. In a typical preparative route, 200 μl of an aqueous solution of $HAuCl_4 \times 3H_2O$ (20 ml of 5 mM) is dissolved in 10 ml milli-Q water and vigorously stirred for 30 min. The $HAuCl_4$ is reduced by quickly adding 1 ml of a freshly prepared aqueous solution of $NaBH_4$ (20 ml of 10 mM) in the absence of any surfactant during the reaction. The formation of Au nanoparticles is reflected on the color change of the solution, from yellowish to red. Upon further stirring (5 min), the color changes to violet, indicating that the initially formed Au nanospheres progressively aggregate into larger interwoven structures giving rise to NWNs. All the solutions were clear and used without further treatment.

Polycrystalline thin film (25 ± 0.3 nm thick) was grown on glass substrate by evaporation of Au metal via electron beam bombardment. Deposition on microscope glass slide at room temperature and pressure $\sim 10^{-7}$ Torr, resulted in the surface shown in the Scanning Electron Microscopy (SEM) image of Fig. 1a carried out on a JEOL JSM 6390LV Scanning Electron Microscope. X-Ray Diffraction (XRD) pattern from the same surface performed with a 12 kW Rigaku DMAX 2400 Series rotating angle diffractometer with Cu Kα radiation is shown in Fig. 1b. Analysis of the XRD patterns (Fig. 1b) by the Scherrer formula allows us to estimate that the polycrystalline TF entails crystallites with an average size of 26.3 nm. The sample thickness was measured with the use of a piezoelectric crystal. This specific film thickness has been chosen so that it can be compared to the effectively equivalent average diameter of the Au NWNs (100 nm multiplied with $p = 75$ % where p is the porosity parameter of the NWNs—as defined later in the text). For the structural characterization of the NWNs (Fig. 2), a JEOL 2100 transmission electron microscope (TEM), operating at an accelerating voltage of 200 kV, was utilized. The morphology and the spatial dimensions of the NWNs were determined via the analysis of low magnification TEM images, as shown in Fig. 2, inset. On the other hand, high-resolution work (HRTEM) allowed the identification of the fcc lattice planes in the Au-based nanostructure (Fig. 2).

The static absorption spectrum of the investigated samples has been measured with a Perkin Elmer LAMBDA 950 UV-VIS spectrometer (shown in Fig. 3). The Au-NWN samples have been examined in the form of aqueous colloidal solution and contained in 2 mm-thick (internal thickness) cuvettes of optical quality. The same samples have been used for the measurements of the ultrafast dynamics described below.

Ultrafast dynamics have been examined by means of ultrafast photo-induced transient transmission. For this purpose, an amplified Ti:Sapphire laser system with 1 kHz repetition rate, 785 nm center wavelength and 30 fs pulse duration was used. Part of the beam is frequency doubled

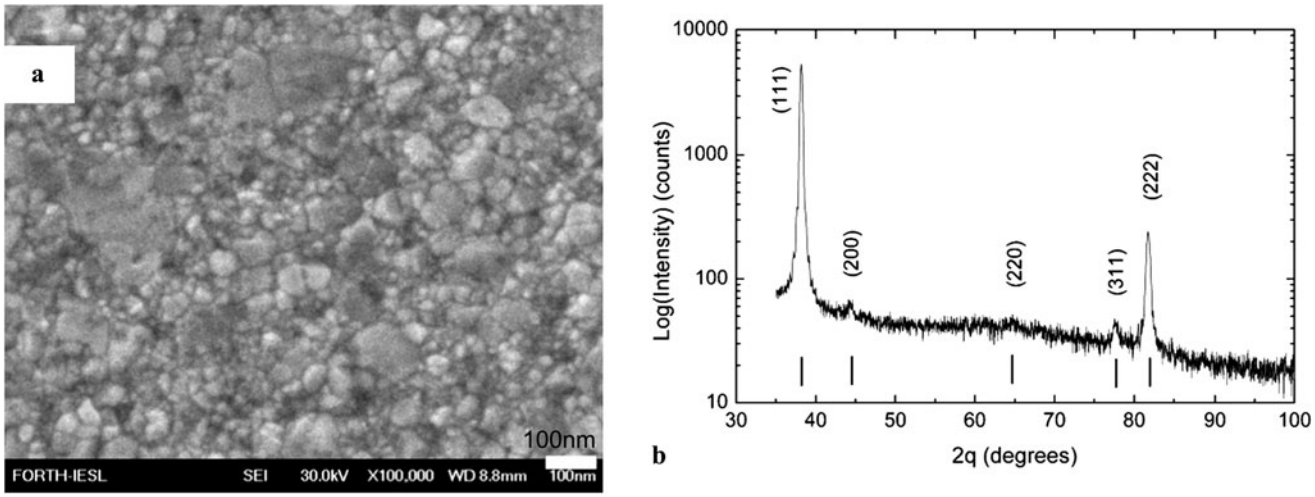

Fig. 1 (**a**) SEM image and (**b**) XRD pattern of the 25 nm thick polycrystalline Au film. *Vertical tick marks* indicate the positions of Bragg reflections indexed on the basis of the fcc unit cell ($\alpha = 4.08$ Å) of Au

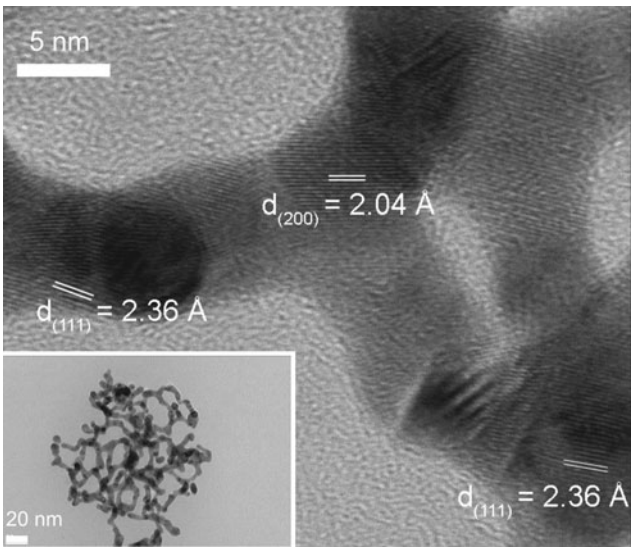

Fig. 2 High-resolution TEM image of Au NWN. *Inset* shows low-magnification TEM image of the whole Au NWN

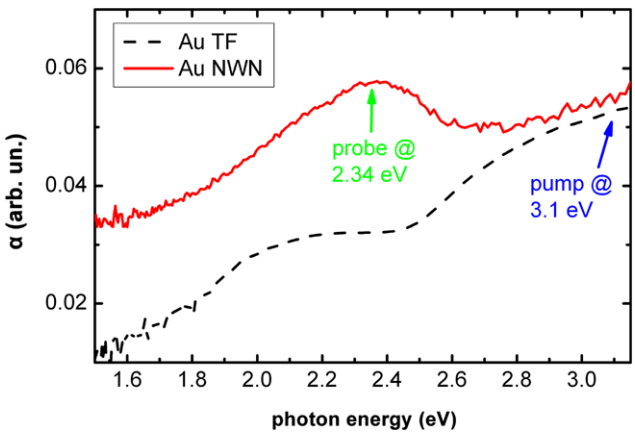

Fig. 3 Absorption coefficient, α, of NWN (*solid line*) and TF (*dashed line*) vs. photon energy. The positions of the pump and the probe photons are indicated with *arrows*

(392 nm = 3.16 eV), using a beta-Barium Borate (BBO) crystal and is then focused on the sample's surface driving it out of equilibrium by nonthermal electron excitation (pump beam). The remaining, temporally delayed beam part, is focused inside a sapphire crystal producing a broadband supercontinuum (white light—WL) pulse [23], which is then focused onto the sample (probe beam). Both beams are spatially overlapped at the sample's surface. The beam diameters on the sample as measured with a CMOS camera are typically 120 μm FWHM for the pump and 50 μm FWHM for the probe beam. Both beams have a nearly Gaussian spatial intensity distribution. The incident fluence of the probe beam is always kept much smaller ($\gg$100 times) than that of the pump beam. The transmitted WL beam is passed through a prism to disperse the wavelengths. The thus dispersed WL supercontinuum is passed through a vertically oriented slit of variable lateral position and of variable aperture, therefore allowing the selection of the central wavelength to be probed and its desired bandwidth (typically ∼10 nm broad). Then, the transmitted probe beam is focused onto a photodiode for the lock-in measurements. A flip-up mirror is occasionally used to divert the probe beam into a fiber spectrometer in order to characterize its spectral properties (wavelength and bandwidth). Transient changes in the differential transmission ΔT were obtained by means of the lock-in detection scheme. The lock-in amplifier is locked to a chopper frequency and phase with the chopper placed to chop the pump beam. In order to increase the sensitivity of the measured signal on the electronic temperature of the samples, the probe photon energy has to lie close to the interband transition threshold for the case of the TF [24] (2.47 eV)

and close to the Au plasmon band for the general case of nanoparticles [25] (in our case NWN—2.34 eV). Therefore, from the probe supercontinuum that is incident onto the sample, we chose to detect the photon energy centered at 2.34 eV (with FWHM of 0.02 eV).

As will be discussed in the next section, the ultrafast electron dynamics depend on the electron temperature. Therefore, all measurements and the subsequent analysis have been evaluated with respect to the same absorbed laser energy *per atom* during the excitation (pump) process. For this, we used the volume concentration of Au in each of the colloidal samples (10^{-4} mol/L) and the volumetric density of bulk Au (19.3 g/cm^3).

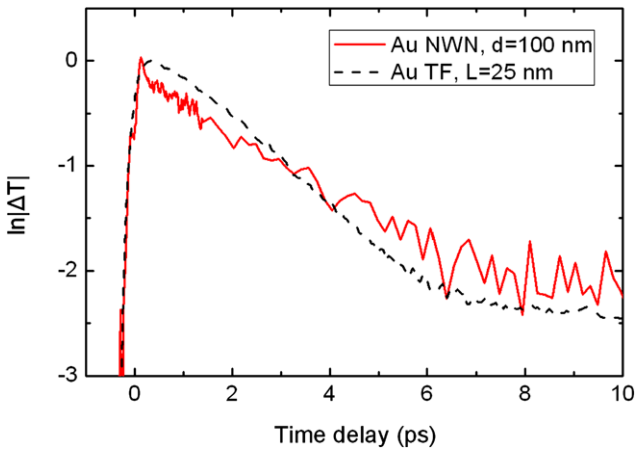

Fig. 4 Transient (pump-probe) transmission traces of 100 nm diameter Au NWN (*red solid line*) and 25 nm thick TF (*black dashed line*)

3 Results and discussion

Conventional and high-resolution TEM images of Au NWNs are shown in Fig. 2. The NWNs consist of clusters of nanoparticles (∼10 nm diameter) that interconnect with each other. The majority of the NWN possess a spherical shape with an average overall diameter of roughly 100 nm (Fig. 2 inset). From high magnification images (Fig. 2), the lattice fringes originating from the fcc Au lattice planes, such as those belonging to the (111) and (200) families, indicate that the NWN are the result of coalescence due to van der Waals interactions of the as-grown single crystalline Au nanoparticles (NPs) in aqueous media. The NPs out of which the network branches are composed are attached one to another at random orientation, giving rise to characteristic kinks in the structure. Our HRTEM images cannot resolve whether such morphological modulation involves coherent interfacial connectivity, pertaining common lattice planes across neighboring Au nanocrystals. However, grain boundary connectivity at the nearby kinks may involve various types of defects such as twins and stacking faults as it has been observed before in similar noble metal nanostructures [26–28]. Absorption spectra of both NWN and TF are shown in Fig. 3. By fitting a Gaussian function plus a fifth-order polynomial background to the NWN absorption spectrum we find that the surface plasmon resonance peak is at (2.34 ± 0.01) eV. We chose a Gaussian function because of the inhomogeneous contributions to the plasmon peak by the relatively broad size and shape distribution of the NWN and a polynomial function for the simulation of the background nonplasmonic contributions to the absorption. As we find by comparison with the fitting results, the excitation (pump) beam centered at 3.16 eV does not excite the plasmon and, therefore, we do not expect such effects to modify the electron kinetics.

The traces of the time resolved transmission ΔT are shown in Fig. 4. We observe that ΔT is negative for the case of the TF. This has been observed in the past in similar experiments [24, 29]. It has been ascribed to the broadened (due to the elevated electron temperature) electron distribution and the resulting reduction of electron occupation at states below the Fermi energy (along with an increase of electron occupation at states above the Fermi energy). The probe beam with a photon energy 2.34 eV excites electrons from the d-bands to states just below the Fermi energy where the electron occupation is now reduced. Therefore, the probability of such transitions is now (at $t > 0$) increased leading to increased absorption, and consequently to reduced transmission (i.e. $\Delta T < 0$) as confirmed in our work. In this specific probe photon energy, we prefer to study the ΔT of the thin film and refrain from analysis of the ΔR as this exhibits a bipolar nature (i.e. the temporal trace changes sign—a fact arising from the nonthermal nature of the electron distribution at early delay times following excitation) that would complicate the analysis [29]. On the other hand, ΔT is positive for the case of the Au NWNs. Our findings for the Au NWNs demonstrate an analogy with small metallic nanoparticles where the peak of the plasmon is reduced with increasing temperature [30]. Therefore, we attribute the positive change, ΔT, to the decrease of the amplitude of the plasmon resonance peak with increasing electron temperature [30] that is caused by the laser excitation. The temporal responses shown in Fig. 4 can be categorized in distinct physical processes depending on the temporal window. Specifically:

(a) In the sub-ps temporal window, the physical mechanism that prevails is the e-e scattering interaction that leads to thermalization of the initially nonthermal electron distribution [24, 31]. This mechanism mainly influences the rise of the temporal traces. As seen in Fig. 4, the temporal trace for the Au TF $|\Delta T|$ rises slower and reaches its maximum value a few 100 fs later than that of the Au NWN. The shorter rise time in the NWN in our case and

in nanoparticles in general is due to the increased e-e scattering [8] arising from the volume confinement (increased surface/volume ratio) which leads to faster establishment of an electronic temperature that is given by a well-defined Fermi–Dirac distribution. Further analysis of this effect in our particular systems is beyond the scope of the present work.

(b) At later time delays, electron–phonon (e-ph) interaction and energy transport mechanisms prevail. An exponential decay in the order of a few ps follows as the thermalized electrons cool by energy transfer toward the lattice via e-ph interaction [9]. At the same time, transport mechanisms dissipate the energy from the initially illuminated volume toward the rest of the material volume via hot electron-induced energy transport [12, 32]. To justify the consideration of electron transport in the decay of the measured signal, we note that although the excitation (pump) process mainly involves d-band electrons, this process results to the Fermi smearing of the electron distribution by promoting d-electrons below the Fermi energy to s-electrons above it [33]. Furthermore, using a probe photon energy, tuned to the interband transition and assuming that the d-electron population is essentially not changed, it is justified to assume that with the chosen probe beam photon energy we monitor the changes in the electron occupation in the vicinity of the Fermi level which results from the excitation of the d-electrons. Thus, for the probe photon energy used in our experiments the dielectric function *changes* can be very well described by the changes in the electron distribution around the Fermi level, which in turn are reflected in the transport of the delocalized electrons and their energy dissipation dynamics. Therefore, in view of the above considerations, we base our interpretation on a macroscopic model (developed later in the text), much related to the Drude model, because it covers the major relaxation processes underlying our experiments.

Coherent vibrational motion was not observed in our measurements as has been observed before either in spherical [9, 10] or in ellipsoidal [34] nanoparticles where the contribution of the coherent electron–phonon interaction manifests itself by an oscillatory signal with a period in the several ps window. In our case, due to the rather large size and shape distribution of the Au NWN, the coherent contribution of different sizes is averaged and any oscillatory contributions to the signal are washed out.

(c) After ∼7 ps all signals have decayed to almost their initial values as before excitation. At these time intervals, slower mechanisms occur such as phonon–phonon (ph-ph) interaction that equilibrates the temperature throughout the lattice [35, 36] and heat transport towards the surrounding medium [9, 13], which proceeds in the timescale of several 100 ps. These processes mainly contribute in the small remaining signal (<10 % of the maximum) after 10 ps, their dynamical evolution is very slow when compared to the processes examined here, and are beyond the scope of this work as well.

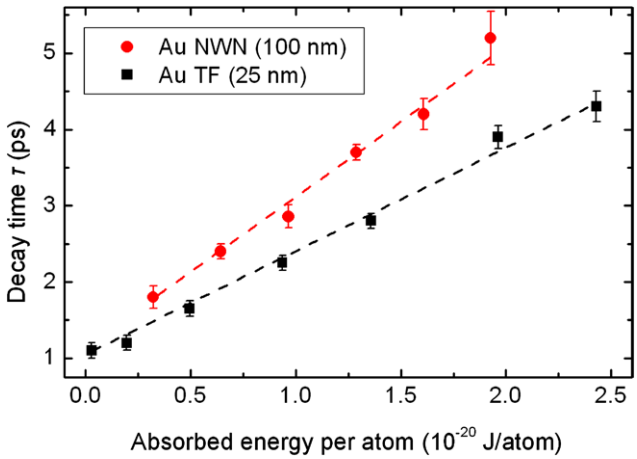

Fig. 5 Transient transmission decay times as a function of absorbed energy per atom for Au NWN (*red circles*) and 25 nm thick TF (*black squares*). *Dashed lines* are a guide to the eye

In order to evaluate and compare the ultrafast dynamics in the examined systems, we have to consider the same excitation conditions because electron-lattice cooling depends on the excitation intensity [36]. Additionally, we take into consideration the morphological differences of the two systems, namely that the TF is solid while on the other hand the NWN is a heavily porous system. Therefore, the proper condition for direct comparison of the ultrafast dynamics in the two systems entails the same absorbed pump energy *per atom*. This is performed and shown in Fig. 5 where we plot the decay time, τ, for both systems as a function of absorbed pump energy *per atom*. The decay times are extracted by assuming single exponential decay ($\sim e^{-t/\tau}$) on the measured transient transmission traces, shown in Fig. 4. The fitting has been restricted to the region 1 ps $< t <$ 7 ps for both cases. The comparison of e-ph coupling strength can be done in the low excitation limit (i.e., low lattice temperature rise) [37]. From Fig. 5, we find that both systems in the low excitation regime tend to have similar decay times, therefore, implying a similar e-ph interaction time. This observation confirms the previously reported shape and size independence of the e-ph coupling strength for Au nanoparticles with sizes ≥10 nm [38]. As the excitation intensity is increased, τ increases differently for the different systems examined. The increasing τ with increasing excitation intensity is due to the temperature-dependent electron heat capacity [32]. Since the pump-beam penetration depth is 17 nm [39], and the spatial extend of both samples is greater than 17 nm, both systems are inhomogenously excited giving rise to a temperature gradient and subsequently leading to energy

transport [12, 32]. Because of the perpetual electron random motion, "hot" electrons will transport toward initially "cold" (unexcited) regions, while their place is going to be taken by "cold" electrons that happen to transport from the "cold" regions toward the "hot" (laser-excited) region. This way by the intermixing of "hot" with "cold" electrons, energy dissipation occurs and contributes to the observed dynamics. Additionally, heat transport away from the metal into the surrounding medium (water for the NWN and glass substrate from one side and air from the other side for the case of the TF) can also contribute to the dynamics of the systems.

Since the thermal conductivity of Au (319 $\mathrm{W\,m^{-1}\,K^{-1}}$ [40]) is much larger than those of water (0.561 $\mathrm{W\,m^{-1}\,K^{-1}}$ [40]) and glass (1.1 $\mathrm{W\,m^{-1}\,K^{-1}}$ [40]), respectively, we consider that energy dissipation occurs preferentially via transport of energy *inside* the sample (be it either NWN or TF) rather than transport of energy from the sample toward the surrounding medium. When comparing the NWN with the TF, we find that the decay times, τ, are consistently shorter in the TF for all the used excitation fluences. In the case of the rigid morphology of the TF, the energy dissipation occurs freely without any confinement. However, this is not the case for the porous NWNs. In the NWN, the special network structure imposes restrictions to the electron transport, and consequently the energy dissipation away from the excited region. In addition, Chirea et al. [21] have observed an increased catalytic activity in similar Au NWN structures. They attributed this behavior on the increased number of "corners and edges". These morphological features serve as localization centers for the conduction electrons either through increased electron-surface scattering due to the increased local importance of the surface-to-volume ratio, or through electron trapping due to the increased confinement imposed by the boundaries. Both mechanisms contribute to a reduction in the transport efficiency of the hot electrons and, therefore, may contribute to the increase of the observed decay times for the case of the NWNs.

To investigate the interplay between the above processes, we performed simulations, based on the well-known one-dimensional (1D) model of Anisimov et al. [41] where we have taken the e-ph coupling strength to be $G = 2.2 \times 10^{10}\ \mathrm{W\,cm^{-3}\,K^{-1}}$ [24].

In our approach, the NWN is modeled as a superposition of parallel Au-layers (films) separated by a layer of empty space (vacuum) from each other. For this structure, both the electronic heat capacity (C_e) and the thermal conductivity (K) are assumed to have the following spatial dependence form:

$$C_\mathrm{e} = \lambda_\mathrm{e} T_\mathrm{e}(z,t) = \eta_\mathrm{e}(z)\lambda_{\mathrm{e}0} T_\mathrm{e}(z,t) \quad (1)$$

$$K = \eta_K(z) K_0 \quad (2)$$

where T_e is the electron temperature, η_e and η_K are form factors describing the spatial dependence of the proportionality constant λ_e and K ($\lambda_{\mathrm{e}0} = 71.5\ \mathrm{J\,m^{-3}\,K^{-2}}$ [24] and $K_0 = 318\ \mathrm{W\,m^{-1}\,K^{-1}}$ [24] are the parameters for the electronic heat capacity and the thermal conductivity for Au, respectively; z is a spatial variable perpendicular to the surface and t is the time).

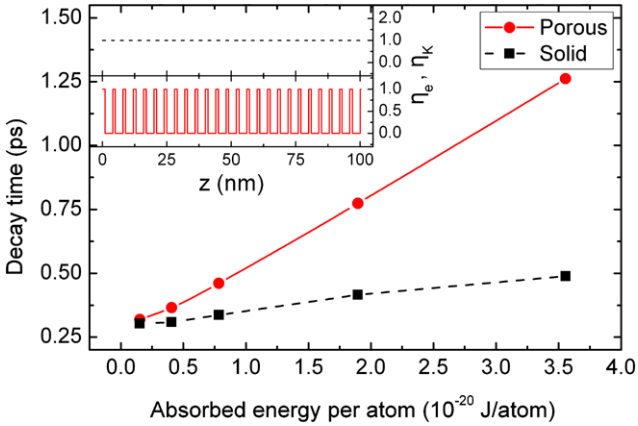

Fig. 6 Theoretical calculation of decay times, using the two temperature model, of a porous (*red circles*) and a solid (*black squares*) film. *Inset*: the spatial dependence of η_e and η_K form factors for the two cases

In our approximation, we assume the following bimodal expressions for η_e and η_K:

- $\eta_\mathrm{e} = \eta_{\mathrm{e,Au}}$; $\eta_K = \eta_{K,\mathrm{Au}}$ for z within a Au-layer and (3)
- $\eta_\mathrm{e} = \eta_{\mathrm{e,V}}$; $\eta_K = \eta_{K,\mathrm{V}}$ for z within a vacuum-layer. (4)

In our calculations, we used $\eta_{\mathrm{e,Au}} = \eta_{K,\mathrm{Au}} = 1$ and $\eta_{\mathrm{e,V}} = 0\eta_{K,\mathrm{V}} = 1$, as shown in inset of Fig. 6. The frequency of alternating values 0 and 1 of the form factors η_e and η_K is implemented by the porosity p of the system. This is defined as the percentage of void in the total space occupied by the Au NWN in one dimension. The value $p = 75$ % has been used for our simulations and has been estimated from the TEM images of Fig. 2. Additionally, the extracted value of $p = 75$ % has been used in order to define the effective diameter of the Au NWN so that the electron transport dynamics can be compared in two systems (a porous and a solid one) having to travel effectively equivalent distances. Calculated decay times as a function of laser fluence (Fig. 6) show a qualitative agreement with the experimental results: the decay times of the porous system are always larger than the solid one, while when decreasing the excitation fluence they tend to acquire similar values. By varying the e-ph coupling constant by two orders of magnitude, decay times did not present considerable change; for that reason and in conjunction with the simulation results in the low excitation regime, we confirm that, in contrast to transport, the e-ph coupling factor does not depend on porosity. Therefore, our simulations verify our experimental findings in a qualitative manner and allow us to demonstrate for the first time that porosity is a significant parameter in the morphology of Au NWNs, which in turn affects the electron transport.

4 Conclusions

In summary, a new type of three-dimensional Au nanowire networks was synthesized with the purpose to probe the influence of their complex morphology on the hot electron transport after excitation by ultrashort laser pulses. Ultrafast pump-probe spectroscopy allowed us to compare the electron dynamics between Au nanowire networks and Au dense thin films with effectively equivalent thickness. It provided evidence that the hot electron transport in the nanowire networks is slower than that in the dense film. Our observations are attributed to the inherent porous structure of the nanowire networks that imposes restrictions to the transport of the hot electrons. The complex morphology of the nanostructure tends to localize the conduction electrons due to the increased numbers of edges and corners that serve as dead ends and trapping centers. The results put forward the significance of the porosity as a parameter to allow manipulation of the ultrafast electron dynamics of complex, three-dimensional open framework nanostructures.

Acknowledgements This work was carried out at the Ultraviolet Laser Facility operating at IESL-FORTH with support from the EC project "Laserlab-Europe II" (FP7-Infrastructures-2008-1, Grant Agreement No: 228334). The authors thank A. Manousaki and L. Papoutsakis for their expert assistance in obtaining SEM and XRD data and the European Commission for financial support through the Marie-Curie Transfer of Knowledge program NANOTAIL (Grant no. MTKD-CT-2006-042459). AGK thanks the University of Southampton (nanousrg) for financial support and the Research Council UK (RCUK) for a Roberts fellowship.

References

1. C. Burda, X.B. Chen, R. Narayanan, M.A. El-Sayed, Chem. Rev. **105**, 1025 (2005)
2. S. Link, M.A. El-Sayed, Int. Rev. Phys. Chem. **19**, 409 (2000)
3. Y.N. Xia, P.D. Yang, Y.G. Sun, Y.Y. Wu, B. Mayers, B. Gates, Y.D. Yin, F. Kim, Y.Q. Yan, Adv. Mater. **15**, 353 (2003)
4. I. Gur, N.A. Fromer, M.L. Geier, A.P. Alivisatos, Science **310**, 462 (2005)
5. I. Gur, N.A. Fromer, C.-P. Chen, A.G. Kanaras, A.P. Alivisatos, Nano Lett. **7**, 409 (2006)
6. R. Narayanan, M.A. El-Sayed, Nano Lett. **4**, 1343 (2004)
7. J. Hohlfeld, J.G. Muller, S.S. Wellershoff, E. Matthias, Appl. Phys. B **64**, 387 (1997)
8. C. Voisin, D. Christofilos, P.A. Loukakos, N. Del Fatti, F. Vallee, J. Lerme, M. Gaudry, E. Cottancin, M. Pellarin, M. Broyer, Phys. Rev. B **69**, 195416 (2004)
9. C. Voisin, N. Del Fatti, D. Christofilos, F. Vallee, J. Phys. Chem. B **105**, 2264 (2001)
10. S. Stagira, M. Nisoli, S. De Silvestri, A. Stella, P. Tognini, P. Cheyssac, R. Kofman, Chem. Phys. **251**, 259 (2000)
11. A. Stella, M. Nisoli, S. DeSilvestri, O. Svelto, G. Lanzani, P. Cheyssac, R. Kofman, Phys. Rev. B **53**, 15497 (1996)
12. M. Bonn, D.N. Denzler, S. Funk, M. Wolf, S.S. Wellershoff, J. Hohlfeld, Phys. Rev. B **61**, 1101 (2000)
13. S. Link, D.J. Hathcock, B. Nikoobakht, M.A. El-Sayed, Adv. Mater. **15**, 393 (2003)
14. L. Manna, R. Krahne, G. Morello, A. Figuerola, C. George, S. Deka, Phys. Rep. **501**, 75 (2011)
15. X.G. Peng, L. Manna, W.D. Yang, J. Wickham, E. Scher, A. Kadavanich, A.P. Alivisatos, Nature **404**, 59 (2000)
16. G. Ramanath, J. D'Arcy-Gall, T. Maddanimath, A.V. Ellis, P.G. Ganesan, R. Goswami, A. Kumar, K. Vijayamohanan, Langmuir **20**, 5583 (2004)
17. A.G. Kanaras, C. Sonnichsen, H.T. Liu, A.P. Alivisatos, Nano Lett. **5**, 2164 (2005)
18. H.A. Day, D. Bartczak, N. Fairbairn, E. McGuire, M. Ardakani, A.E. Porter, A.G. Kanaras, CrystEngComm **12**, 4312 (2010)
19. Y. Lu, J.Y. Huang, C. Wang, S.H. Sun, J. Lou, Nat. Nanotechnol. **5**, 218 (2010)
20. A. Murugadoss, A. Chattopadhyay, J. Phys. Chem. C **112**, 11265 (2008)
21. M. Chirea, A. Freitas, B.S. Vasile, C. Ghitulica, C.N. Pereira, F. Silva, Langmuir **27**, 3906 (2011)
22. L.M. Liz-Marzan, M. Yang, R. Alvarez-Puebla, H.S. Kim, P. Aldeanueva-Potel, N.A. Kotov, Nano Lett. **10**, 4013 (2010)
23. A. Brodeur, S.L. Chin, J. Opt. Soc. Am. B **16**, 637 (1999)
24. J. Hohlfeld, S.S. Wellershoff, J. Gudde, U. Conrad, V. Jahnke, E. Matthias, Chem. Phys. **251**, 237 (2000)
25. N. Del Fatti, F. Vallee, C. Flytzanis, Y. Hamanaka, A. Nakamura, Chem. Phys. **251**, 215 (2000)
26. W.Q. Wang, W.S. Liang, C.Y. Geng, Nanoscale Res. Lett. **4**, 684 (2009)
27. C. Wang, Y. Wei, H. Jiang, S. Sun, Nano Lett. **10**, 2121 (2010)
28. Q. Yuan, X. Wang, Nanoscale **2**, 2328 (2010)
29. C.-K. Sun, F. Vallee, L.H. Acioli, E.P. Ippen, J.G. Fujimoto, Phys. Rev. B **50**, 15337 (1994)
30. R.H. Doremus, J. Chem. Phys. **40**, 2389 (1964)
31. C.-K. Sun, F. Vallee, L. Acioli, E.P. Ippen, J.G. Fujimoto, Phys. Rev. B **48**, 12365 (1993)
32. S.D. Brorson, J.G. Fujimoto, E.P. Ippen, Phys. Rev. Lett. **59**, 1962 (1987)
33. R.W. Schoenlein, W.Z. Lin, J.G. Fujimoto, G.L. Eesley, Phys. Rev. Lett. **58**, 1680 (1987)
34. M. Perner, S. Gresilon, J. Maerz, G. von Plessen, J. Feldmann, J. Porstendorfer, K.-J. Berg, G. Berg, Phys. Rev. Lett. **85**, 792 (2000)
35. C.A. Paddock, G.L. Eesley, J. Appl. Phys. **60**, 285 (1986)
36. H.E. Elsayedali, T. Juhasz, G.O. Smith, W.E. Bron, Phys. Rev. B **43**, 4488 (1991)
37. S.L. Logunov, T.S. Ahmadi, M.A. El-Sayed, J.T. Khoury, R.L. Whetten, J. Phys. Chem. B **101**, 3713 (1997)
38. S. Link, C. Burda, M.B. Mohamed, B. Nikoobakht, M.A. El-Sayed, Phys. Rev. B **61**, 6086 (2000)
39. L.G. Schulz, J. Opt. Soc. Am. **44**, 357 (1954)
40. Tables of Physical & Chemical Constants 16th edn. (1995) 2.3.7 Thermal conductivities. Kaye & Laby Online. Version 1.0 (2005) www.kayelaby.npl.co.uk
41. S.I. Anisimov, B.L. Kapeliovich, T.L. Perelman, Sov. Phys. JETP **39**, 375 (1974)